THE JOURNAL OF PHYSICAL CHEMISTRY LETTERS
A JOURNAL OF THE AMERICAN CHEMICAL SOCIETY

pubs.acs.org/JPCL Letter

Non-empirical Mixing Coefficient for Hybrid XC Functionals from Analysis of the XC Kernel

Zhandos A. Moldabekov,* Mani Lokamani, Jan Vorberger, Attila Cangi, and Tobias Dornheim

Cite This: J. Phys. Chem. Lett. 2023, 14, 1326−1333 Read Online

ACCESS | Metrics & More | Article Recommendations | Supporting Information

ABSTRACT: We present an analysis of the static exchange-correlation (XC) kernel computed from hybrid functionals with a single mixing coefficient such as PBE0 and PBE0−1/3. We break down the hybrid XC kernels into the exchange and correlation parts using the Hartree−Fock functional, the exchange-only PBE, and the correlation-only PBE. This decomposition is combined with exact data for the static XC kernel of the uniform electron gas and an Airy gas model within a subsystem functional approach. This gives us a tool for the non-empirical choice of the mixing coefficient under ambient and extreme conditions. Our analysis provides physical insights into the effect of the variation of the mixing coefficient in hybrid functionals, which is of immense practical value. The presented approach is general and can be used for other types of functionals like screened hybrids.

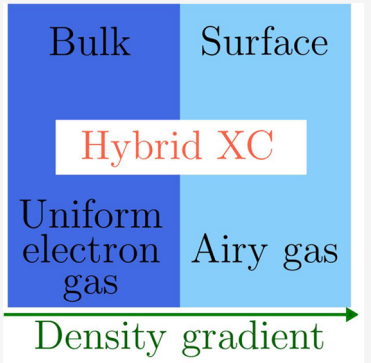

Modern density functional theory (DFT) based on the Kohn−Sham scheme[1] is the most widely used electronic structure method and is routinely applied in computational chemistry, condensed-matter physics, materials science, and related disciplines. The accuracy of a DFT calculation depends strongly on the particular choice of the exchange-correlation (XC) functional.[2] It needs to be approximated and supplied as an external input to any DFT calculations. In this regard, orbital-dependent XC functionals that are defined in the context of the generalized Kohn−Sham density functional (KS-DFT)[3−5] have distinguished practical value for DFT calculations. Furthermore, it is one of the most promising directions in quantum chemistry toward achieving predictable capability with DFT calculations. Commonly used orbital-dependent XC functionals belong to the class of hybrid functionals that mix exact Hartree−Fock (HF) exchange with the exchange energy obtained from a density functional approximation, e.g., on the level of the local density approximation (LDA) and the generalized density approximation (GGA).[6,7] The success of hybrid XC functionals stems from the reduction of the infamous self-interaction (or delocalization) error, which often hinders explicit density XC functionals like LDA and GGA from reaching chemical accuracy.[8] Additionally, hybrid XC functionals enable thermal XC effects[9,10] to be treated more accurately than usual ground-state functionals due to the inherent use of thermally smeared occupation numbers.[11−13] This is particularly important for warm dense matter (WDM),[14−16] which is a state of matter generated for example by laser heating or shock compression at facilities such as the European X-ray Free-Electron Laser (XFEL)[17] and Linac coherent light source (LCLS) at SLAC[18] and naturally occurs in astrophysical objects like the interior of giant planets.[18,19] Important technological applications of WDM include the discovery of novel materials under extreme conditions[20−22] and hot-electron chemistry.[23] Therefore, a rigorous understanding of hybrid XC functionals within the generalized KS-DFT approach is of immense importance for physics and quantum chemistry under both ambient and extreme conditions.

Hybrid XC functionals are typically constructed by combining a certain amount of HF exchange with the exchange energy obtained from an XC approximation. Following Perdew, Ernzerhof, and Burke,[24] hybrid XC functionals are represented as

$$E_{xc}[\rho_\sigma, n] = E_c^{DF}[n] + aE_x^{HF}[\rho_\sigma] + (1 - a)E_x^{DF}[n] \quad (1)$$

where a is termed the mixing parameter and DF is an acronym for density functional. Examples for eq 1 are PBE0[7] with $a = {}^1/_4$ and PBE0−1/3[25] with $a = {}^1/_3$, where $E_{xc}^{DF} = E_{xc}^{PBE}$.[26] To ease the computational cost of PBE0, a screened version of its exchange part was implemented in HSE03[27] and HSE06,[28,29] where the Coulomb interaction $\sim 1/r$ is substituted by a screened interaction $\sim \mathrm{erfc}(\Omega r)/r$, with Ω denoting the screening parameter. Arguably, for solids, these four are the

Received: December 2, 2022
Accepted: January 13, 2023
Published: February 1, 2023

https://doi.org/10.1021/acs.jpclett.2c03670
J. Phys. Chem. Lett. 2023, 14, 1326−1333

most commonly applied and most famous hybrid XC functionals. Furthermore, we refer to the hybrid functionals with an arbitrary mixing coefficient a in eq 1 and with $E_{xc}^{DF} = E_{xc}^{PBE}$ as the PBE0-type functionals.

While a general framework of the KS-DFT with hybrid XC functionals has been rigorously derived by Garrick et al.,[5] the choice of the degree of mixing for solids had remained somewhat intuitive and justified empirically by computing material properties and comparing them with experimental measurements such as lattice constants, bulk moduli, the vacancy formation energy, and atomic data. The usually quoted rationale for the choice of the mixing coefficient is from Perdew et al.,[24] who analyzed atomization errors of typical molecules from the Møller−Plesset perturbation expansion to conjecture $a = {}^1/_4$. Clearly, there is ample room left for the variation of the degree of mixing and of the screening parameter for systems different from molecules under ambient conditions. The situation is particularly unsatisfactory for WDM, where such basic atomic properties like an atomization energy become ill defined due to the smearing of the boundary between bound and free states at high pressure or temperature,[30−33] and where bulk properties such as the vacancy formation energy or bulk moduli cannot be accurately measured due to prevalent extreme conditions. Moreover, the bulk properties of materials like the lattice constant (interparticle distance and/or separation), stress tensor, etc., at high pressures and temperatures often differ significantly from those under ambient conditions. This calls for an approach that allows the rationalization of the choice of the mixing coefficient and screening without employing properties of individual atoms and molecules or other physical properties limited to ambient conditions. At the same time, it is preferable that such a rationale have some connection to properties that are well-defined and measurable in experiments across temperature and pressure regimes. Here we show that the static XC kernel $K_{xc}(q)$ [where q denotes a wavenumber (see eq 2)] can serve this purpose. First, we discuss the $K_{xc}(q)$ of the PBE0-type hybrid functionals by comparing it to archetypal electron gas models[34] to illustrate the concept. Then, we describe how this can be related to the static density response function (susceptibility) $\chi(q)$ that can be measured in experiments via the X-ray Thomson scattering (XRTS) technique.[35,36]

We begin by arguing that the choice of the mixing coefficient can be based on the $K_{xc}(q)$ of the uniform electron gas (UEG),[34,37] which is valid for bulk systems, and on the $K_{xc}(q)$ of the AM05 functional,[38] which incorporates the limit of the Airy gas at large gradients typically close to surface regions. This is demonstrated for the static XC kernel of the PBE0-type functionals by varying the mixing coefficient over a wide range of values. The AM05 functional incorporates the exact exchange energy of the Airy gas and consists of a correlation part that is fitted to reproduce jellium surface energies (because exact quantum Monte Carlo data for the Airy gas are not available). Importantly, the AM05 functional enables an accurate and universal treatment of systems with electronic surfaces.[38,39] Hence, choosing the UEG and jellium surface as reference data for $K_{xc}(q)$ is motivated by the fact that the functionals based on these generic-model systems are more widely applicable for solids than those XC functionals that are fitted to specific materials (see, e.g., refs 26 and 38−41).

First, we recall that the complete information about the density response of a given system of interest is contained in the dynamic density response function, which can be conveniently expressed for homogeneous systems as[34]

$$\chi(\mathbf{q}, \omega) = \frac{\chi_0(\mathbf{q}, \omega)}{1 - [v(q) + K_{xc}(\mathbf{q}, \omega)]\chi_0(\mathbf{q}, \omega)} \tag{2}$$

where $v(q) = 4\pi/q^2$ is the Coulomb potential in reciprocal space and $\chi_0(\mathbf{q}, \omega)$ denotes a known reference function such as the response of the ideal Fermi gas in the case of a UEG or the KS response function $\chi_{KS}(\mathbf{q}, \omega)$ for linear response time-dependent DFT (LR-TDDFT) calculations of materials.[42] The exact density response is then given by the combination of $\chi_0(\mathbf{q}, \omega)$ with the dynamic XC kernel $K_{xc}(\mathbf{q}, \omega)$. We note that the density response function in eq 2 depends on only one wavenumber because we consider a homogeneous system.[34,43] In general, for inhomogeneous systems, the density response function depends on two wavenumbers that are usually expressed as $\mathbf{k} + \mathbf{G}$ and $\mathbf{k} + \mathbf{G}'$ with reciprocal lattice vectors $\mathbf{G}$ and $\mathbf{G}'$, and $\mathbf{k}$ denoting a wave vector restricted to the first Brillouin zone.[43]

The XC kernel can be computed by inverting eq 2 if the density response function is known. To compute the static XC kernel $K_{xc}(\mathbf{q}) = K_{xc}(\mathbf{q}, \omega = 0)$, we perturb the UEG with an external static harmonic perturbation $V_{ext} = 2A\cos(\mathbf{q}\cdot\mathbf{r})$. Then, static density response function $\chi(\mathbf{q})$ (defined by setting $\omega = 0$ in eq 2) is found from the difference $\delta n(\mathbf{r})$ between the perturbed and unperturbed densities:[44−46]

$$\delta n(\mathbf{r}) = 2A\cos(\mathbf{q}\cdot\mathbf{r})\chi(\mathbf{q}) \tag{3}$$

This approach for computing $\chi(q)$ was used for the UEG by Dornheim et al.[47,48] within the path integral Monte Carlo (PIMC) method. Recently, this method has been extended to the KS-DFT and has been illustrated for the UEG and warm dense hydrogen.[45] By doing so, we circumvent the need to compute a second-order functional derivative of the XC functional and, thus, can calculate the static XC kernel across Jacob's ladder.[45] The key ingredient of our analysis is the exact quantum Monte Carlo data for the so-called local field correction (LFC) of the UEG, which is connected to the XC kernel as $G(q) = -K_{xc}(q)/v(q)$ and is commonly used in the quantum theory of the electron liquid.[34,49,50]

The UEG is conveniently described by mean interparticle distance r_s and the reduced temperature $\theta = T/T_F$, where r_s is in units of the Bohr radius and T_F is the Fermi temperature (energy).[51,52] All results are presented in Hartree atomic units. We consider metallic densities and set r_s equal to 2, which is typical for both solids and WDM.[53] The results are presented for the ground state $\theta = 0.01$ with strong electron degeneracy and for the case with partial electron degeneracy $\theta = 1$, i.e., $T = T_F$. The former case corresponds to ambient conditions, and the latter is characteristic of WDM. We note that perturbation amplitude A in eq 3 must be small enough to avoid higher-order nonlinear effects. This aspect was extensively analyzed within the KS-DFT method for the UEG by Moldabekov et al.[54] Furthermore, we drop the vector notation for the wavenumber and set $\mathbf{q}$ in eq 3 to be along the z-axis. We note that the linear response of an UEG depends on only q.

The ABINIT package[55−60] has been used for the KS-DFT calculations of the perturbed free electron gas. The results at $\theta = 0.01$ are presented for $N = 38$ electrons, and those at $\theta = 1.0$ for $N = 14$ electrons. We note that finite-size effects have been extensively investigated in the literature[61−67] and are expected to be small for these conditions. The corresponding cell

https://doi.org/10.1021/acs.jpclett.2c03670
J. Phys. Chem. Lett. 2023, 14, 1326−1333

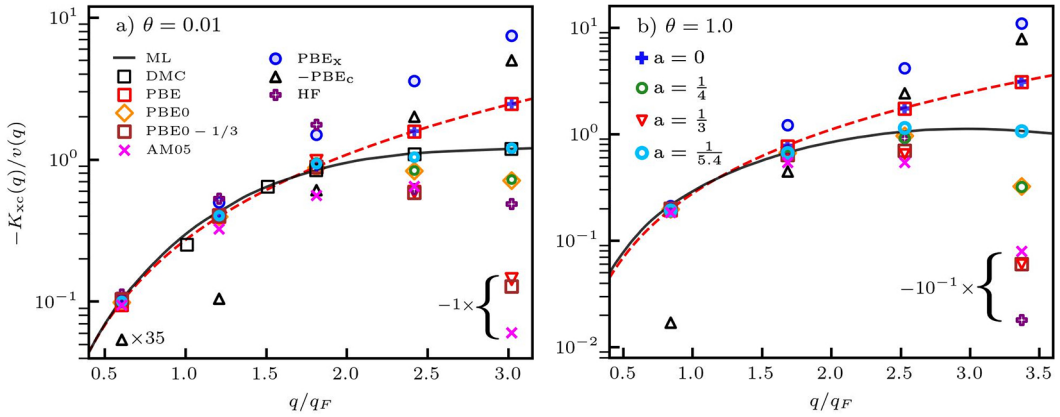

Figure 1. (a) Static XC kernel of the UEG at (a) $\theta = 0.01$ and (b) $\theta = 1$ for $r_s = 2$. The exact diffusion quantum Monte Carlo (DMC) results of Moroni et al.[44] are presented as black squares for $\theta = 0.01$. The solid line is the ML representation of the exact quantum Monte Carlo results by Dornheim et al.[64] The dashed line illustrates the quadratic dependence of the PBE data on q. Mixing parameter a indicates the data obtained by combining the results for kernels from the separate HF, the exchange-only PBE (labeled as PBE_x), and the correlation-only PBE (labeled as PBE_c) calculations as $K_{xc}(q, a) = K_{xc}^{PBE_c}(q) + aK_{xc}^{HF}(q) + (1 - a)K_{xc}^{PBE_x}(q)$. Other symbols correspond to the KS-DFT data computed using PBE, PBE0, PBE0−1/3, and AM05 as described in the text. Some data points are multiplied by a constant factor to better illustrate the results. The corresponding multiplications are explicitly shown next to the curly braces in the graphs.

lengths (L) are 10.839 and 7.7703 Bohr, respectively. The perturbation wavenumber is defined by the length of the main simulation cell as $q = 2\pi j/L$, where $j \geq 1$ is a positive integer number. The number of bands at $\theta = 0.01$ is set to 76, and that at $\theta = 1.0$ to 200. The calculations are performed with periodic boundary conditions and a k-point grid of 8 × 8 × 8. The maximal kinetic energy cutoff is set to 13 hartree. Self-consistent-field cycles for the solution of the Kohn−Sham equations were converged with absolute differences in total energy of $\delta E < 10^{-7}$ Hartree. The perturbation amplitude is set to $A = 0.01$. For a detailed discussion of the convergence with respect to the simulation parameters, see our recent papers.[11,45]

The results for K_{xc} of the UEG for $r_s = 2$ at $\theta = 0.01$ and $\theta = 1.0$ are presented in Figure 1. Remarkably, we find exactly the same trend for both temperatures. In particular, we show K_{xc} values computed using the PBE, PBE0, PBE0−1/3, and AM05 functionals and compare them with the exact diffusion quantum Monte Carlo (DMC) results of Moroni et al. (black squares)[44] at $\theta = 0.01$ as well as with the machine-learning representation (ML) by Dornheim et al.[64] based on an extensive PIMC simulation for the WDM parameters (solid line). The dashed red line illustrates the quadratic q dependence of $K_{xc}(q)$ based on PBE according to the compressibility sum rule.[45] It becomes exact in the limit of $q \to 0$. The results for $K_{xc}(q)$ based on various LDA, GGA, meta-GGA, and hybrid XC functionals, including the data for the PBE, PBE0, PBE0−1/3, and AM05 functionals, were reported in refs 11 and 45. In this work, we break down the PBE0-type functionals into exchange and correlation parts with the aim of obtaining physical insight into how the results change as we vary the mixing coefficient. To that end, we carried out additional calculations using only the HF orbital-dependent functional, only the exchange part of PBE (PBE_x), and only the correlation part of PBE (PBE_c).

Let us start our discussion with the special case of eq 1 with $a = 0$, i.e., without the HF contribution. In this case, eq 1 reduces to the PBE functional. From Figure 1, we infer that the results for the kernels in PBE_x (blue circles) and PBE_c (black triangles) vastly differ from the full PBE data (red squares) and all other results. Thus, we use a logarithmic scale for comparative analysis. The kernels $K_{xc}(q)$ based on PBE_x and PBE_c have opposite signs (PBE_c data are shown with a minus sign). The first numerical observation is that the PBE_x kernel is dominant over the PBE_c kernel in the entire q range, $q \lesssim 3q_F$ (with q_F being the Fermi wavenumber). In particular, when $q < q_F$, the PBE_x kernel is larger than the PBE_c kernel by at least 1 order of magnitude in absolute value. In Figure 1a, the data point at $q \simeq 0.6q_F$ for the PBE_c kernel is multiplied by a factor of 35 for a better illustration. The direct sum of the PBE_x and PBE_c data for the UEG reproduces the results obtained using the full PBE functional, because the XC kernel is equivalent to the second-order functional derivative of the XC functional, and for PBE, we have $E_{xc}^{PBE}[n] = E_x^{PBE}[n] + E_c^{PBE}[n]$.[26]

Next, we consider the case in which $a = {}^1/_4$, which is the definition of the PBE0 functional (depicted using an orange rhombus). For PBE0, one needs to mix in a fraction of HF exchange. The full HF data (purple plus signs) are in close agreement with PBE_x data at $q < 1.5q_F$ with a a maximum at $1.5q_F < q < 2q_F$. At $q > 2q_F$, the HF kernel underestimates $K_{xc}(q)$ compared to the exact quantum Monte Carlo data. Now we add a quarter of the HF kernel, three-quarters of the PBE_x kernel, and the full PBE_c kernel according to eq 1 with $a = {}^1/_4$. The resulting data points (green circles) are in agreement with the data computed using the PBE0 functional. This sanity check confirms that the PBE0 XC kernel for the UEG can be found by adding the exchange and correlation parts computed separately. Figure 1 shows that, on one hand, replacing one-quarter of the PBE_x kernel with one-quarter of the HF kernel significantly reduces the PBE0 kernel at $q > 2q_F$ compared to the exact data for the UEG. On the other hand, this replacement leaves the PBE0 kernel almost unaffected at $q < 2q_F$. The reason for this is the aforementioned observation that the HF kernel is nearly the same as the PBE_x kernel at $q < 2q_F$.

Then, we consider the results of the PBE0−1/3 functional (brown squares). As for PBE0, here we use the static XC kernel data from the separate HF, PBE_x, and PBE_c calculations to combine them according to eq 1 with $a = {}^1/_3$. The result (red inverted triangles) reproduces the data obtained from

https://doi.org/10.1021/acs.jpclett.2c03670
J. Phys. Chem. Lett. 2023, 14, 1326−1333

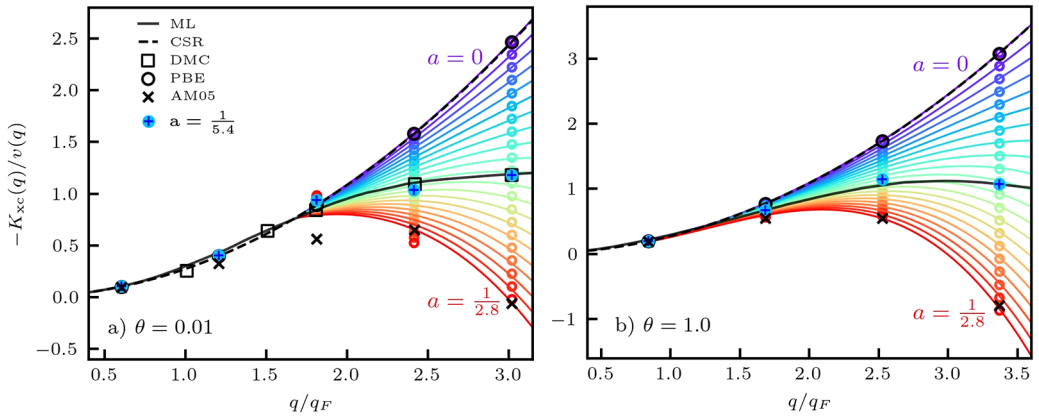

Figure 2. Static XC kernel at (a) $\theta = 0.01$ and (b) $\theta = 1$ for $r_s = 2$. The exact diffusion quantum Monte Carlo (DMC) results of Moroni et al.[44] are presented as black squares for $\theta = 0.01$. The solid line is the ML representation of the exact quantum Monte Carlo data by Dornheim et al.[64] The dashed lines illustrate the quadratic dependence of the PBE data on q in logarithmic scale. Mixing parameter a in eq 1 is varied in the range of $0-{}^1/_{2.8}$. The KS-DFT data corresponding to different a values are presented as circles with different colors, and the corresponding lines depict spline interpolations between these data points. In addition, we show the data points computed using $a = {}^1/_{5.4}$.

independent simulations using the PBE0−1/3 functional (see Figure 1). We observe that the admission of one-third of the HF exchange does not affect the PBE0−1/3 kernel at $q < 2q_F$ due to the close value of the HF kernel and the PBE_x kernel at these wavenumbers. At the same time, the mixing of one-third of the HF exchange leads to a significant reduction of the PBE0−1/3 kernel compared to the exact data for the UEG at $q > 2q_F$. At $q > 3q_F$, the PBE0−1/3 kernel even changes its sign with the increase in the wavenumber (indicated in Figure 1 by multiplication by a negative factor). The reason for that is that the HF kernel reduces with the increase in q at $q > 2q_F$ and thus the difference between the exchange and correlation parts of the PBE0−1/3 kernel decreases and eventually the sign of the kernel changes at $q > 3q_F$.

Therefore, we have established that at $q > 2q_F$ the disagreement between the exact data for the UEG and both PBE0−1/3 and PBE0 increases with an increase in the wavenumber, because the HF kernel decreases with q. On the contrary, Figure 1 shows that the same decreasing trend at $q > 2q_F$ holds for the AM05 kernel (pink crosses). In fact, the agreement of the PBE0 and PBE0−1/3 kernels with the AM05 kernel is much closer than the agreement of the PBE kernel with AM05. This is also the case for the HSE06 and HSE03 kernels, which are screened versions of PBE0.[11] A relevant observation is that AM05 performs as well as PBE0 and HSE06 and much better than PBE for solids and surfaces.[39] The success of AM05 is due to a subsystem functional approach.[68] Within the subsystem functional approach, AM05 mimics the Airy gas model at large density gradients and the UEG model at small density gradients.[38] Indeed, we see that at $q \lesssim 1.5q_F$, AM05 is in agreement with PBE and with the exact data for the UEG. Figure 1 shows that the increase in the mixing coefficient from $a = {}^1/_4$ (used for PBE0) to $a = {}^1/_3$ (used for PBE0−1/3) leads to the closer agreement of the PBE0-type kernel with the AM05 kernel.

After this illustration of our approach for the analysis of PBE0-type functionals for the examples of $a = {}^1/_4$ and $a = {}^1/_3$, we now use the HF, PBE_x, and PBE_c kernels to investigate the PBE0-type kernel for a wide range of values of mixing parameter a. In particular, we achieve an excellent agreement with the exact data for the UEG at the considered wavenumbers by choosing $a = {}^1/_{5.4}$ as illustrated for both $\theta = 0.01$ and $\theta = 1$ in Figure 1 (light blue circles). In Figure 2, we scan a values from $a = 0$ to $a = {}^1/_{2.8}$ to show that the corresponding PBE0-type kernel changes from the PBE kernel to the AM05 kernel with an increase in a at $q > 2q_F$ and remains in good agreement with the exact data for the UEG at $q < 2q_F$.

An important conclusion we draw from these results is that the mixing coefficient for PBE0-type functionals can be chosen using the XC kernel from the UEG model or from AM05, which incorporates the Airy gas model within the subsystem functional approach at large density gradients. These two models are archetypal for electrons in the bulk[26,69] and in the surface regions[38,39,41,70] of solids. The functionals that are based on such generic models are termed non-empirical functionals because they are valid for a larger range of materials than functionals created for some specific systems.[24,26,39] In this way, we provide a theoretical device for constructing hybrid functionals that are non-empirical and that apply for both solid-state systems and WDM. Indeed, one could perform a similar analysis for screened hybrid functionals by varying screening parameter Ω. Moreover, the static XC kernel of the UEG based on HF, PBE_x, and PBE_c functionals can be calculated over a wide range of densities and temperatures to find the optimal parameters of the hybrid XC functionals such as the mixing coefficient. Additionally, this method can be used with a greater degree of freedom in terms of range-separated functionals,[71−75] a subgroup of hybrid XC functionals that provide more flexibility in tuning the exchange energy component

An important observation is that a small change in mixing coefficient a does not lead to a drastic change in the XC kernel as shown in Figure 2, where we vary a with a step size of ${}^1/_{56}$ from 0 to ${}^1/_{2.8}$. Thus, it is not expected that, e.g., the choice $a = {}^1/_{2.8}$ (which closely reproduces the AM05 kernel) yields results significantly different from those for $a = {}^1/_3$ (used in PBE0−1/3) when applied to solids. On the contrary, the presented approach is particularly valuable for applications beyond ambient conditions where surface properties are less relevant, which is the case for liquid metals, dense plasmas, and WDM. For example, there is no need to take the surface properties of WDM into consideration, because warm dense samples generated by laser heating or shock compression do not have

https://doi.org/10.1021/acs.jpclett.2c03670
J. Phys. Chem. Lett. 2023, 14, 1326−1333

a clearly distinguishable surface. Thus, our approach yields a rationale for choosing, e.g., $a = {}^{1}/_{5.4}$ at metallic densities, which should yield a better description of the bulk properties.

We are convinced that our new insights into the non-empirical mixing coefficient in hybrid functionals will be useful for a number of applications both under ambient conditions and in the WDM regime. In particular, we stress that the XC kernel is very important in its own right and constitutes the key input for the computation of material properties such as effective potentials,[34,76−78] quantum fluid dynamics,[79−82] or LR-TDDFT simulations of real materials[42] and plasmonics.[83] A particularly interesting possibility is the experimental verification of our work for the hybrid XC kernel in XRTS experiments in WDM.[35] XRTS is a standard tool of diagnostics of WDM, and measurements can be performed at both small $q < 2q_F$ and large $q > 2q_F$ wavenumbers.[84−86] In fact, the XRTS signal is proportional to the dynamic structure factor of the electrons convolved with the probe function. Recently, it has been shown that a two-sided Laplace transform of the measured XRTS intensity can be used to compute the imaginary-time density−density correlation function with significantly reduced experimental noise.[87] This allows one to subsequently find static density response function $\chi(q)$ via the imaginary-time version of the fluctuation−dissipation theorem.[36] Thus, the static XC kernel that has been shown here is a suitable quantity for determining the mixing coefficient of hybrid functionals non-empirically. In addition, it can also be probed in XRTS measurements of matter under extreme conditions.

■ ASSOCIATED CONTENT

Supporting Information

The Supporting Information is available free of charge at https://pubs.acs.org/doi/10.1021/acs.jpclett.2c03670.

Transparent Peer Review report available (PDF)

■ AUTHOR INFORMATION

Corresponding Author

Zhandos A. Moldabekov − *Center for Advanced Systems Understanding (CASUS), Helmholtz-Zentrum Dresden-Rossendorf (HZDR), D-02826 Görlitz, Germany;* orcid.org/0000-0002-9725-9208; Email: z.moldabekov@hzdr.de

Authors

Mani Lokamani − *Information Services and Computing, Helmholtz-Zentrum Dresden-Rossendorf (HZDR), D-01328 Dresden, Germany*

Jan Vorberger − *Institute of Radiation Physics, Helmholtz-Zentrum Dresden-Rossendorf (HZDR), D-01328 Dresden, Germany*

Attila Cangi − *Center for Advanced Systems Understanding (CASUS), Helmholtz-Zentrum Dresden-Rossendorf (HZDR), D-02826 Görlitz, Germany*

Tobias Dornheim − *Center for Advanced Systems Understanding (CASUS), Helmholtz-Zentrum Dresden-Rossendorf (HZDR), D-02826 Görlitz, Germany*

Complete contact information is available at: https://pubs.acs.org/10.1021/acs.jpclett.2c03670

Notes

The authors declare no competing financial interest.

■ ACKNOWLEDGMENTS

This work was funded by the Center for Advanced Systems Understanding (CASUS), which is financed by Germany's Federal Ministry of Education and Research (BMBF) and by the Saxon state government out of the State budget approved by the Saxon State Parliament. The authors gratefully acknowledge computation time at the Norddeutscher Verbund für Hoch- und Höchstleistungsrechnen (HLRN) under Grant shp00026 and on the Bull Cluster at the Center for Information Services and High Performance Computing (ZIH) at Technische Universität Dresden. The authors thank Henrik Schulz and Jens Lasch for providing very helpful support on high-performance computing at HZDR.

■ REFERENCES

(1) Kohn, W.; Sham, L. J. Self-consistent equations including exchange and correlation effects. *Phys. Rev.* **1965**, *140*, A1133−A1138.

(2) Burke, K. Perspective on density functional theory. *J. Chem. Phys.* **2012**, *136*, 150901.

(3) Seidl, A.; Görling, A.; Vogl, P.; Majewski, J. A.; Levy, M. Generalized Kohn-Sham schemes and the band-gap problem. *Phys. Rev. B* **1996**, *53*, 3764−3774.

(4) Kümmel, S.; Kronik, L. Orbital-dependent density functionals: Theory and applications. *Rev. Mod. Phys.* **2008**, *80*, 3−60.

(5) Garrick, R.; Natan, A.; Gould, T.; Kronik, L. Exact Generalized Kohn-Sham Theory for Hybrid Functionals. *Phys. Rev. X* **2020**, *10*, 021040.

(6) Becke, A. D. Density-functional thermochemistry. III. The role of exact exchange. *J. Chem. Phys.* **1993**, *98*, 5648−5652.

(7) Adamo, C.; Barone, V. Toward reliable density functional methods without adjustable parameters: The PBE0 model. *J. Chem. Phys.* **1999**, *110*, 6158−6170.

(8) Cohen, A. J.; Mori-Sánchez, P.; Yang, W. Insights into Current Limitations of Density Functional Theory. *Science* **2008**, *321*, 792−794.

(9) Karasiev, V. V.; Calderin, L.; Trickey, S. B. Importance of finite-temperature exchange correlation for warm dense matter calculations. *Phys. Rev. E* **2016**, *93*, 063207.

(10) Ramakrishna, K.; Dornheim, T.; Vorberger, J. Influence of finite temperature exchange-correlation effects in hydrogen. *Phys. Rev. B* **2020**, *101*, 195129.

(11) Moldabekov, Z. A.; Lokamani, M.; Vorberger, J.; Cangi, A.; Dornheim, T. Assessing the accuracy of hybrid exchange-correlation functionals for the density response of warm dense electrons. *arXiv* **2022**, DOI: 10.48550/arXiv.2211.11688.

(12) Witte, B. B. L.; Fletcher, L. B.; Galtier, E.; Gamboa, E.; Lee, H. J.; Zastrau, U.; Redmer, R.; Glenzer, S. H.; Sperling, P. Warm Dense Matter Demonstrating Non-Drude Conductivity from Observations of Nonlinear Plasmon Damping. *Phys. Rev. Lett.* **2017**, *118*, 225001.

(13) Ravasio, A.; Bethkenhagen, M.; Hernandez, J.-A.; Benuzzi-Mounaix, A.; Datchi, F.; French, M.; Guarguaglini, M.; Lefevre, F.; Ninet, S.; Redmer, R.; Vinci, T. Metallization of Shock-Compressed Liquid Ammonia. *Phys. Rev. Lett.* **2021**, *126*, 025003.

(14) Dornheim, T.; Groth, S.; Bonitz, M. The uniform electron gas at warm dense matter conditions. *Phys. Rep.* **2018**, *744*, 1−86.

(15) Graziani, F., Desjarlais, M. P., Redmer, R., Trickey, S. B., Eds. *Frontiers and challenges in warm dense matter*; Springer International Publishing, 2014.

(16) Bonitz, M.; Dornheim, T.; Moldabekov, Z. A.; Zhang, S.; Hamann, P.; Kählert, H.; Filinov, A.; Ramakrishna, K.; Vorberger, J. Ab initio simulation of warm dense matter. *Physics of Plasmas* **2020**, *27*, 042710.

(17) Tschentscher, T.; Bressler, C.; Grünert, J.; Madsen, A.; Mancuso, A. P.; Meyer, M.; Scherz, A.; Sinn, H.; Zastrau, U. Photon Beam Transport and Scientific Instruments at the European XFEL. *Applied Sciences* **2017**, *7*, 592.

(18) He, Z.; Rödel, M.; Lütgert, J.; Bergermann, A.; Bethkenhagen, M.; Chekrygina, D.; Cowan, T. E.; Descamps, A.; French, M.; Galtier, E.; Gleason, A. E.; Glenn, G. D.; Glenzer, S. H.; Inubushi, Y.; Hartley, N. J.; Hernandez, J.-A.; Heuser, B.; Humphries, O. S.; Kamimura, N.; Katagiri, K.; Khaghani, D.; Lee, H. J.; McBride, E. E.; Miyanishi, K.; Nagler, B.; Ofori-Okai, B.; Ozaki, N.; Pandolfi, S.; Qu, C.; Ranjan, D.; Redmer, R.; Schoenwaelder, C.; Schuster, A. K.; Stevenson, M. G.; Sueda, K.; Togashi, T.; Vinci, T.; Voigt, K.; Vorberger, J.; Yabashi, M.; Yabuuchi, T.; Zinta, L. M. V.; Ravasio, A.; Kraus, D. Diamond formation kinetics in shock-compressed C-H-O samples recorded by small-angle x-ray scattering and x-ray diffraction. *Sci. Adv.* **2022**, *8*, eabo0617.

(19) Benuzzi-Mounaix, A.; Mazevet, S.; Ravasio, A.; Vinci, T.; Denoeud, A.; Koenig, M.; Amadou, N.; Brambrink, E.; Festa, F.; Levy, A.; Harmand, M.; Brygoo, S.; Huser, G.; Recoules, V.; Bouchet, J.; Morard, G.; Guyot, F.; de Resseguier, T.; Myanishi, K.; Ozaki, N.; Dorchies, F.; Gaudin, J.; Leguay, P. M.; Peyrusse, O.; Henry, O.; Raffestin, D.; Pape, S. L.; Smith, R.; Musella, R. Progress in warm dense matter study with applications to planetology. *Phys. Scr.* **2014**, *T161*, 014060.

(20) Lazicki, A.; McGonegle, D.; Rygg, J. R.; Braun, D. G.; Swift, D. C.; Gorman, M. G.; Smith, R. F.; Heighway, P. G.; Higginbotham, A.; Suggit, M. J.; Fratanduono, D. E.; Coppari, F.; Wehrenberg, C. E.; Kraus, R. G.; Erskine, D.; Bernier, J. V.; Mc-Naney, J. M.; Rudd, R. E.; Collins, G. W.; Eggert, J. H.; Wark, J. S. Metastability of diamond ramp-compressed to 2 terapascals. *Nature* **2021**, *589*, 532−535.

(21) Kritcher, A. L.; Swift, D. C.; Döppner, T.; Bachmann, B.; Benedict, L. X.; Collins, G. W.; DuBois, J. L.; Elsner, F.; Fontaine, G.; Gaffney, J. A.; Hamel, S.; Lazicki, A.; Johnson, W. R.; Kostinski, N.; Kraus, D.; MacDonald, M. J.; Maddox, B.; Martin, M. E.; Neumayer, P.; Nikroo, A.; Nilsen, J.; Remington, B. A.; Saumon, D.; Sterne, P. A.; Sweet, W.; Correa, A. A.; Whitley, H. D.; Falcone, R. W.; Glenzer, S. H. A measurement of the equation of state of carbon envelopes of white dwarfs. *Nature* **2020**, *584*, 51−54.

(22) Kraus, D.; Vorberger, J.; Pak, A.; Hartley, N. J.; Fletcher, L. B.; Frydrych, S.; Galtier, E.; Gamboa, E. J.; Gericke, D. O.; Glenzer, S. H.; Granados, E.; MacDonald, M. J.; MacKinnon, A. J.; McBride, E. E.; Nam, I.; Neumayer, P.; Roth, M.; Saunders, A. M.; Schuster, A. K.; Sun, P.; van Driel, T.; Döppner, T.; Falcone, R. W. Formation of diamonds in laser-compressed hydrocarbons at planetary interior conditions. *Nature Astronomy* **2017**, *1*, 606−611.

(23) Brongersma, M. L.; Halas, N. J.; Nordlander, P. Plasmon-induced hot carrier science and technology. *Nat. Nanotechnol.* **2015**, *10*, 25−34.

(24) Perdew, J. P.; Ernzerhof, M.; Burke, K. Rationale for mixing exact exchange with density functional approximations. *J. Chem. Phys.* **1996**, *105*, 9982−9985.

(25) Cortona, P. Note: Theoretical mixing coefficients for hybrid functionals. *J. Chem. Phys.* **2012**, *136*, 086101.

(26) Perdew, J. P.; Burke, K.; Ernzerhof, M. Generalized gradient approximation made simple. *Phys. Rev. Lett.* **1996**, *77*, 3865−3868.

(27) Heyd, J.; Scuseria, G. E.; Ernzerhof, M. Hybrid functionals based on a screened Coulomb potential. *J. Chem. Phys.* **2003**, *118*, 8207−8215.

(28) Heyd, J.; Scuseria, G. E.; Ernzerhof, M. Erratum: hybrid functionals based on a screened Coulomb potential - J. Chem. Phys. 118, 8207 (2003). *J. Chem. Phys.* **2006**, *124*, 219906.

(29) Krukau, A. V.; Vydrov, O. A.; Izmaylov, A. F.; Scuseria, G. E. Influence of the exchange screening parameter on the performance of screened hybrid functionals. *J. Chem. Phys.* **2006**, *125*, 224106.

(30) Böhme, M.; Moldabekov, Z. A.; Vorberger, J.; Dornheim, T. Static Electronic Density Response of Warm Dense Hydrogen: Ab Initio Path Integral Monte Carlo Simulations. *Phys. Rev. Lett.* **2022**, *129*, 066402.

(31) Hu, S. X.; Bishel, D. T.; Chin, D. A.; Nilson, P. M.; Karasiev, V. V.; Golovkin, I. E.; Gu, M.; Hansen, S. B.; Mihaylov, D. I.; Shaffer, N. R.; Zhang, S.; Walton, T. Probing atomic physics at ultrahigh pressure using laser-driven implosions. *Nat. Commun.* **2022**, *13*, 6780.

(32) Massacrier, G.; Böhme, M.; Vorberger, J.; Soubiran, F.; Militzer, B. Reconciling ionization energies and band gaps of warm dense matter derived with ab initio simulations and average atom models. *Phys. Rev. Research* **2021**, *3*, 023026.

(33) Hu, S. X.; Karasiev, V. V.; Recoules, V.; Nilson, P. M.; Brouwer, N.; Torrent, M. Interspecies radiative transition in warm and superdense plasma mixtures. *Nat. Commun.* **2020**, *11*, 1989.

(34) Giuliani, G.; Vignale, G.*Quantum theory of the electron liquid*; Masters Series in Physics and Astronomy; Cambridge University Press, 2005.

(35) Glenzer, S. H.; Redmer, R. X-ray Thomson scattering in high energy density plasmas. *Rev. Mod. Phys.* **2009**, *81*, 1625.

(36) Dornheim, T.; Moldabekov, Z.; Tolias, P.; Böhme, M.; Vorberger, J. Physical insights from imaginary-time density−density correlation functions. *arXiv* **2022**, DOI: 10.48550/arXiv.2209.02254.

(37) Loos, P.-F.; Gill, P. M. W. The uniform electron gas. *Comput. Mol. Sci.* **2016**, *6*, 410−429.

(38) Armiento, R.; Mattsson, A. E. Functional designed to include surface effects in self-consistent density functional theory. *Phys. Rev. B* **2005**, *72*, 085108.

(39) Mattsson, A. E.; Armiento, R.; Paier, J.; Kresse, G.; Wills, J. M.; Mattsson, T. R. The AM05 density functional applied to solids. *J. Chem. Phys.* **2008**, *128*, 084714.

(40) Paier, J.; Marsman, M.; Kresse, G. Why does the B3LYP hybrid functional fail for metals? *J. Chem. Phys.* **2007**, *127*, 024103.

(41) Vitos, L.; Johansson, B.; Kollár, J.; Skriver, H. L. Exchange energy in the local Airy gas approximation. *Phys. Rev. B* **2000**, *62*, 10046−10050.

(42) Marques, M.; Maitra, N.; Nogueira, F.; Gross, E.; Rubio, A.*Fundamentals of Time-Dependent Density Functional Theory*; Lecture Notes in Physics; Springer: Berlin, 2012.

(43) Ullrich, C. A.*Time-Dependent Density-Functional Theory: Concepts and Applications*; Oxford University Press, 2011.

(44) Moroni, S.; Ceperley, D. M.; Senatore, G. Static Response and Local Field Factor of the Electron Gas. *Phys. Rev. Lett.* **1995**, *75*, 689−692.

(45) Moldabekov, Z. A.; Böhme, M.; Vorberger, J.; Blaschke, D.; Dornheim, T. Ab initio Static Exchange-Correlation Kernel across Jacob's Ladder without functional derivatives. *arXiv* **2022**, DOI: 10.48550/arXiv.2209.00928.

(46) Dornheim, T.; Böhme, M.; Moldabekov, Z. A.; Vorberger, J.; Bonitz, M. Density response of the warm dense electron gas beyond linear response theory: Excitation of harmonics. *Phys. Rev. Research* **2021**, *3*, 033231.

(47) Dornheim, T.; Vorberger, J.; Bonitz, M. Nonlinear Electronic Density Response in Warm Dense Matter. *Phys. Rev. Lett.* **2020**, *125*, 085001.

(48) Dornheim, T.; Groth, S.; Vorberger, J.; Bonitz, M. Permutation-blocking path-integral Monte Carlo approach to the static density response of the warm dense electron gas. *Phys. Rev. E* **2017**, *96*, 023203.

(49) Kugler, A. A. Theory of the local field correction in an electron gas. *J. Stat. Phys.* **1975**, *12*, 35.

(50) Dornheim, T.; Cangi, A.; Ramakrishna, K.; Böhme, M.; Tanaka, S.; Vorberger, J. Effective static approximation: A fast and reliable tool for warm-dense matter theory. *Phys. Rev. Lett.* **2020**, *125*, 235001.

(51) Skiff, F.; Wurtele, J.*Plasma: at the frontier of science discovery*; 2017.

(52) Ott, T.; Thomsen, H.; Abraham, J. W.; Dornheim, T.; Bonitz, M. Recent progress in the theory and simulation of strongly correlated plasmas: phase transitions, transport, quantum, and magnetic field effects. *Eur. Phys. J. D* **2018**, *72*, 84.

(53) Ramakrishna, K.; Cangi, A.; Dornheim, T.; Baczewski, A.; Vorberger, J. First-principles modeling of plasmons in aluminum under ambient and extreme conditions. *Phys. Rev. B* **2021**, *103*, 125118.

(54) Moldabekov, Z.; Vorberger, J.; Dornheim, T. Density Functional Theory Perspective on the Nonlinear Response of

https://doi.org/10.1021/acs.jpclett.2c03670
J. Phys. Chem. Lett. 2023, 14, 1326−1333

Correlated Electrons across Temperature Regimes. *J. Chem. Theory Comput.* **2022**, *18*, 2900−2912.
(55) Gonze, X.; Amadon, B.; Antonius, G.; Arnardi, F.; Baguet, L.; Beuken, J.-M.; Bieder, J.; Bottin, F.; Bouchet, J.; Bousquet, E.; Brouwer, N.; Bruneval, F.; Brunin, G.; Cavignac, T.; Charraud, J.-B.; Chen, W.; Côté, M.; Cottenier, S.; Denier, J.; Geneste, G.; Ghosez, P.; Giantomassi, M.; Gillet, Y.; Gingras, O.; Hamann, D. R.; Hautier, G.; He, X.; Helbig, N.; Holzwarth, N.; Jia, Y.; Jollet, F.; Lafargue-Dit-Hauret, W.; Lejaeghere, K.; Marques, M. A. L.; Martin, A.; Martins, C.; Miranda, H. P. C.; Naccarato, F.; Persson, K.; Petretto, G.; Planes, V.; Pouillon, Y.; Prokhorenko, S.; Ricci, F.; Rignanese, G.-M.; Romero, A. H.; Schmitt, M. M.; Torrent, M.; van Setten, M. J.; Van Troeye, B.; Verstraete, M. J.; Zérah, G.; Zwanziger, J. W. The Abinit project: Impact, environment and recent developments. *Comput. Phys. Commun.* **2020**, *248*, 107042.
(56) Romero, A. H.; Allan, D. C.; Amadon, B.; Antonius, G.; Applencourt, T.; Baguet, L.; Bieder, J.; Bottin, F.; Bouchet, J.; Bousquet, E.; Bruneval, F.; Brunin, G.; Caliste, D.; Côté, M.; Denier, J.; Dreyer, C.; Ghosez, P.; Giantomassi, M.; Gillet, Y.; Gingras, O.; Hamann, D. R.; Hautier, G.; Jollet, F.; Jomard, G.; Martin, A.; Miranda, H. P. C.; Naccarato, F.; Petretto, G.; Pike, N. A.; Planes, V.; Prokhorenko, S.; Rangel, T.; Ricci, F.; Rignanese, G.-M.; Royo, M.; Stengel, M.; Torrent, M.; van Setten, M. J.; Van Troeye, B.; Verstraete, M. J.; Wiktor, J.; Zwanziger, J. W.; Gonze, X. ABINIT: Overview, and focus on selected capabilities. *J. Chem. Phys.* **2020**, *152*, 124102.
(57) Gonze, X.; Jollet, F.; Abreu Araujo, F.; Adams, D.; Amadon, B.; Applencourt, T.; Audouze, C.; Beuken, J.-M.; Bieder, J.; Bokhanchuk, A.; Bousquet, E.; Bruneval, F.; Caliste, D.; Côté, M.; Dahm, F.; Da Pieve, F.; Delaveau, M.; Di Gennaro, M.; Dorado, B.; Espejo, C.; Geneste, G.; Genovese, L.; Gerossier, A.; Giantomassi, M.; Gillet, Y.; Hamann, D.; He, L.; Jomard, G.; Laflamme Janssen, J.; Le Roux, S.; Levitt, A.; Lherbier, A.; Liu, F.; Lukačević, I.; Martin, A.; Martins, C.; Oliveira, M.; Poncé, S.; Pouillon, Y.; Rangel, T.; Rignanese, G.-M.; Romero, A.; Rousseau, B.; Rubel, O.; Shukri, A.; Stankovski, M.; Torrent, M.; Van Setten, M.; Van Troeye, B.; Verstraete, M.; Waroquiers, D.; Wiktor, J.; Xu, B.; Zhou, A.; Zwanziger, J. Recent developments in the ABINIT software package. *Comput. Phys. Commun.* **2016**, *205*, 106−131.
(58) Gonze, X.; Amadon, B.; Anglade, P.-M.; Beuken, J.-M.; Bottin, F.; Boulanger, P.; Bruneval, F.; Caliste, D.; Caracas, R.; Côté, M.; Deutsch, T.; Genovese, L.; Ghosez, P.; Giantomassi, M.; Goedecker, S.; Hamann, D.; Hermet, P.; Jollet, F.; Jomard, G.; Leroux, S.; Mancini, M.; Mazevet, S.; Oliveira, M.; Onida, G.; Pouillon, Y.; Rangel, T.; Rignanese, G.-M.; Sangalli, D.; Shaltaf, R.; Torrent, M.; Verstraete, M.; Zerah, G.; Zwanziger, J. ABINIT: First-principles approach to material and nanosystem properties. *Comput. Phys. Commun.* **2009**, *180*, 2582−2615.
(59) Gonze, X.; Rignanese, G.-M.; Verstraete, M.; Beuken, J.-M.; Pouillon, Y.; Caracas, R.; Jollet, F.; Torrent, M.; Zerah, G.; Mikami, M.; Ghosez, P.; Veithen, M.; Raty, J.-Y.; Olevano, V.; Bruneval, F.; Reining, L.; Godby, R.; Onida, G.; Allan, D. H. A brief introduction to the ABINIT software package. *Z. Kristallogr. - Cryst. Mater.* **2005**, *220*, 558−562.
(60) Gonze, X.; Beuken, J.-M.; Caracas, R.; Detraux, F.; Fuchs, M.; Rignanese, G.-M.; Sindic, L.; Verstraete, M.; Zerah, G.; Jollet, F.; Torrent, M.; Roy, A.; Mikami, M.; Ghosez, P.; Raty, J.-Y.; Allan, D. First-principles computation of material properties: The ABINIT software project. *Comput. Mater. Sci.* **2002**, *25*, 478−492.
(61) Chiesa, S.; Ceperley, D. M.; Martin, R. M.; Holzmann, M. Finite-Size Error in Many-Body Simulations with Long-Range Interactions. *Phys. Rev. Lett.* **2006**, *97*, 076404.
(62) Dornheim, T.; Groth, S.; Sjostrom, T.; Malone, F. D.; Foulkes, W. M. C.; Bonitz, M. Ab Initio Quantum Monte Carlo Simulation of the Warm Dense Electron Gas in the Thermodynamic Limit. *Phys. Rev. Lett.* **2016**, *117*, 156403.
(63) Dornheim, T.; Vorberger, J. Overcoming finite-size effects in electronic structure simulations at extreme conditions. *J. Chem. Phys.* **2021**, *154*, 144103.
(64) Dornheim, T.; Vorberger, J.; Groth, S.; Hoffmann, N.; Moldabekov, Z.; Bonitz, M. The static local field correction of the warm dense electron gas: An ab initio path integral Monte Carlo study and machine learning representation. *J. Chem. Phys.* **2019**, *151*, 194104.
(65) Moldabekov, Z. A.; Dornheim, T.; Cangi, A. Thermal excitation signals in the inhomogeneous warm dense electron gas. *Sci. Rep.* **2022**, *12*, 1093.
(66) Moldabekov, Z.; Dornheim, T.; Böhme, M.; Vorberger, J.; Cangi, A. The relevance of electronic perturbations in the warm dense electron gas. *J. Chem. Phys.* **2021**, *155*, 124116.
(67) Moldabekov, Z.; Dornheim, T.; Vorberger, J.; Cangi, A. Benchmarking exchange-correlation functionals in the spin-polarized inhomogeneous electron gas under warm dense conditions. *Phys. Rev. B* **2022**, *105*, 035134.
(68) Armiento, R.; Mattsson, A. E. Subsystem functionals in density-functional theory: Investigating the exchange energy per particle. *Phys. Rev. B* **2002**, *66*, 165117.
(69) Perdew, J. P.; Ruzsinszky, A.; Csonka, G. I.; Vydrov, O. A.; Scuseria, G. E.; Constantin, L. A.; Zhou, X.; Burke, K. Restoring the density-gradient expansion for exchange in solids and surfaces. *Phys. Rev. Lett.* **2008**, *100*, 136406.
(70) Kohn, W.; Mattsson, A. E. Edge Electron Gas. *Phys. Rev. Lett.* **1998**, *81*, 3487−3490.
(71) Toulouse, J.; Colonna, F. m. c.; Savin, A. Long-range−short-range separation of the electron-electron interaction in density-functional theory. *Phys. Rev. A* **2004**, *70*, 062505.
(72) Iikura, H.; Tsuneda, T.; Yanai, T.; Hirao, K. A long-range correction scheme for generalized-gradient-approximation exchange functionals. *J. Chem. Phys.* **2001**, *115*, 3540−3544.
(73) Yanai, T.; Tew, D. P.; Handy, N. C. A new hybrid exchange−correlation functional using the Coulomb-attenuating method (CAM-B3LYP). *Chem. Phys. Lett.* **2004**, *393*, 51−57.
(74) Akinaga, Y.; Ten-no, S. Range-separation by the Yukawa potential in long-range corrected density functional theory with Gaussian-type basis functions. *Chem. Phys. Lett.* **2008**, *462*, 348−351.
(75) Seth, M.; Ziegler, T. Range-Separated Exchange Functionals with Slater-Type Functions. *J. Chem. Theory Comput.* **2012**, *8*, 901−907.
(76) Dornheim, T.; Tolias, P.; Moldabekov, Z. A.; Cangi, A.; Vorberger, J. Effective electronic forces and potentials from ab initio path integral Monte Carlo simulations. *J. Chem. Phys.* **2022**, *156*, 244113.
(77) Kukkonen, C. A.; Chen, K. Quantitative electron-electron interaction using local field factors from quantum Monte Carlo calculations. *Phys. Rev. B* **2021**, *104*, 195142.
(78) Moldabekov, Z.; Kählert, H.; Dornheim, T.; Groth, S.; Bonitz, M.; Ramazanov, T. S. Dynamical structure factor of strongly coupled ions in a dense quantum plasma. *Physical Review E: Statistical Physics, Plasmas, Fluids, and Related Interdisciplinary Topics* **2019**, *99*, 053203.
(79) Diaw, A.; Murillo, M. A viscous quantum hydrodynamics model based on dynamic density functional theory. *Sci. Rep.* **2017**, *7*, 15352.
(80) Moldabekov, Z. A.; Bonitz, M.; Ramazanov, T. S. Theoretical foundations of quantum hydrodynamics for plasmas. *Physics of Plasmas* **2018**, *25*, 031903.
(81) Moldabekov, Z. A.; Dornheim, T.; Gregori, G.; Graziani, F.; Bonitz, M.; Cangi, A. Towards a Quantum Fluid Theory of Correlated Many-Fermion Systems from First Principles. *SciPost Phys.* **2022**, *12*, 62.
(82) Graziani, F.; Moldabekov, Z.; Olson, B.; Bonitz, M. Shock physics in warm dense matter: A quantum hydrodynamics perspective. *Contrib. Plasma Phys.* **2022**, *62*, e202100170.
(83) Della Sala, F. Orbital-free methods for plasmonics: Linear response. *J. Chem. Phys.* **2022**, *157*, 104101.
(84) Preston, T. R.; Appel, K.; Brambrink, E.; Chen, B.; Fletcher, L. B.; Fortmann-Grote, C.; Glenzer, S. H.; Granados, E.; Göde, S.; Konôpková, Z.; Lee, H. J.; Marquardt, H.; McBride, E. E.; Nagler, B.; Nakatsutsumi, M.; Sperling, P.; Witte, B. B. L.; Zastrau, U.

https://doi.org/10.1021/acs.jpclett.2c03670
J. Phys. Chem. Lett. 2023, 14, 1326−1333

Measurements of the momentum-dependence of plasmonic excitations in matter around 1 Mbar using an X-ray free electron laser. *Appl. Phys. Lett.* **2019**, *114*, 014101.

(85) Glenzer, S. H.; Fletcher, L. B.; Galtier, E.; Nagler, B.; Alonso-Mori, R.; Barbrel, B.; Brown, S. B.; Chapman, D. A.; Chen, Z.; Curry, C. B.; Fiuza, F.; Gamboa, E.; Gauthier, M.; Gericke, D. O.; Gleason, A.; Goede, S.; Granados, E.; Heimann, P.; Kim, J.; Kraus, D.; MacDonald, M. J.; Mackinnon, A. J.; Mishra, R.; Ravasio, A.; Roedel, C.; Sperling, P.; Schumaker, W.; Tsui, Y. Y.; Vorberger, J.; Zastrau, U.; Fry, A.; White, W. E.; Hasting, J. B.; Lee, H. J. Matter under extreme conditions experiments at the Linac Coherent Light Source. *Journal of Physics B: Atomic, Molecular and Optical* **2016**, *49*, 092001.

(86) Frydrych, S.; Vorberger, J.; Hartley, N. J.; Schuster, A. K.; Ramakrishna, K.; Saunders, A. M.; van Driel, T.; Falcone, R. W.; Fletcher, L. B.; Galtier, E.; Gamboa, E. J.; Glenzer, S. H.; Granados, E.; MacDonald, M. J.; MacKinnon, A. J.; McBride, E. E.; Nam, I.; Neumayer, P.; Pak, A.; Voigt, K.; Roth, M.; Sun, P.; Gericke, D. O.; Döppner, T.; Kraus, D. Demonstration of X-ray Thomson scattering as diagnostics for miscibility in warm dense matter. *Nat. Commun.* **2020**, *11*, 2620.

(87) Dornheim, T.; Böhme, M.; Kraus, D.; Döppner, T.; Preston, T. R.; Moldabekov, Z. A.; Vorberger, J. Accurate temperature diagnostics for matter under extreme conditions. *Nat. Commun.* **2022**, *13*, 7911.

https://doi.org/10.1021/acs.jpclett.2c03670
J. Phys. Chem. Lett. 2023, 14, 1326−1333